Chapter 19
Dielectric Structures

Abstract Dielectric structures, in particular periodic dielectric structures are treated. A general one-dimensional model is developed describing Bragg mirrors. Examples for photonic band gap materials in one, two and three dimensions are given. Different types of dielectric cavities and microscopic resonators including Fabry–Pérot and whispering gallery resonators are treated. Quantum electrodynamic physical effects from light matter coupling such as Purcell effect and strong coupling are treated.

19.1 Photonic Band Gap Materials

Layered structures of dielectric materials with different index of refraction are used as optical elements such as filters or reflection and anti-reflection coatings [1326]. In this section we discuss the use of such concepts in one-, two- and three-dimensional photonic band gap materials.

19.1.1 Introduction

A structure with a so-called *photonic* band gap (PBG) exhibits an energy range (color range) in which photons cannot propagate in any direction. In the photonic band gap, there are no optical modes, no spontaneous emission and no vacuum (zero-field) fluctuations. We recollect that spontaneous emission is not a necessary occurrence: Looking at Fermi's golden rule (19.18) for the transition probability integrated over all final states

$$w(E) = \frac{2\pi}{\hbar} |M|^2 \rho_f(E), \tag{19.1}$$

we see that the decay rate depends on the density ρ_f of final states at energy E. In the case of spontaneous emission, this is the (vacuum) density D_{em} of electromagnetic

Fig. 19.1 *Right* electromagnetic dispersion with a forbidden gap at the wavevector of the periodicity. *Left* Electron-wave dispersion typical of a direct-gap semiconductor. When the photonic band gap straddles the electronic band gap, electron–hole recombination into photons is inhibited since the photons have no place to go (zero final density of states)
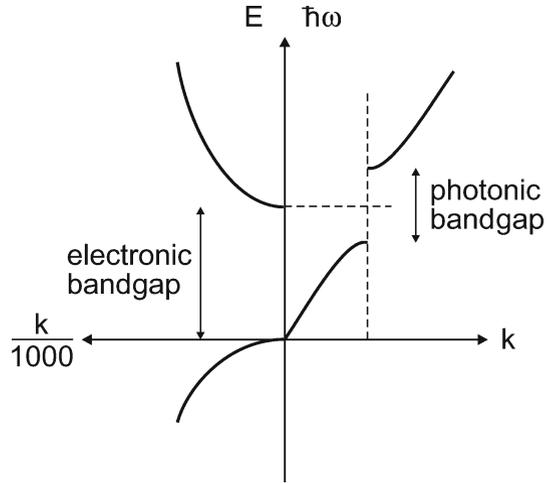
modes (per energy per volume) that varies $\propto \omega^2$:

$$D_{em}(E) = \frac{8\pi}{(hc)^3} E^2. \tag{19.2}$$

In a homogeneous optical medium c must be replaced with c/n (cmp. Sect. 10.2.3).

If the band gap of a PBG is tuned to the electronic gap of a semiconductor, the spontaneous emission, and also induced emission, can be suppressed. Thus, one mode has to be left by 'doping' the structure. In this mode all emission will disappear and an efficient single-mode (monochromatic) LED or 'zero-threshold' laser could be built. A schematic comparison of the band structure of electrons and photons is given in Fig. 19.1.

19.1.2   General 1D Scattering Theory

The formation of a photonic band gap in a one-dimensional dielectric can be calculated to a large extent analytically and thus with direct insight. Let $n(x)$ be the spatially varying index of refraction (no losses or nonlinear optical effects). The one-dimensional wave equation (Helmholtz equation) reads for the electric field E

$$\frac{\partial^2 E(x)}{\partial x^2} + n^2(x) \frac{\omega^2}{c^2} E(x) = 0. \tag{19.3}$$

A comparison with a one-dimensional Schrödinger equation

$$\frac{\partial^2 \Psi(x)}{\partial x^2} - \frac{2m}{\hbar^2} \left[V(x) - E \right] \Psi(x) = 0 \tag{19.4}$$

shows that the Helmholtz equation corresponds to the quantum-mechanical wave equation of zero external potential V and a spatially modulated mass, i.e. a case that is usually not considered.

Let us consider now the amplitude a_k of the k eigenvector. The eigenvalue is then ω_k. The one-dimensional mode density $\rho(\omega)$ (per energy and per unit length) is

$$\rho(\omega) = \frac{\mathrm{d}k}{\mathrm{d}\omega}, \tag{19.5}$$

which is the inverse of the group velocity.

We follow one-dimensional scattering theory as presented in [1327]. At this point we do not rely on any specific form of $n(x)$ (Fig. 19.2a). The (complex) transmission coefficient t for any index structure is

$$t = x + \mathrm{i}y = \sqrt{T} \, \exp(\mathrm{i}\phi), \tag{19.6}$$
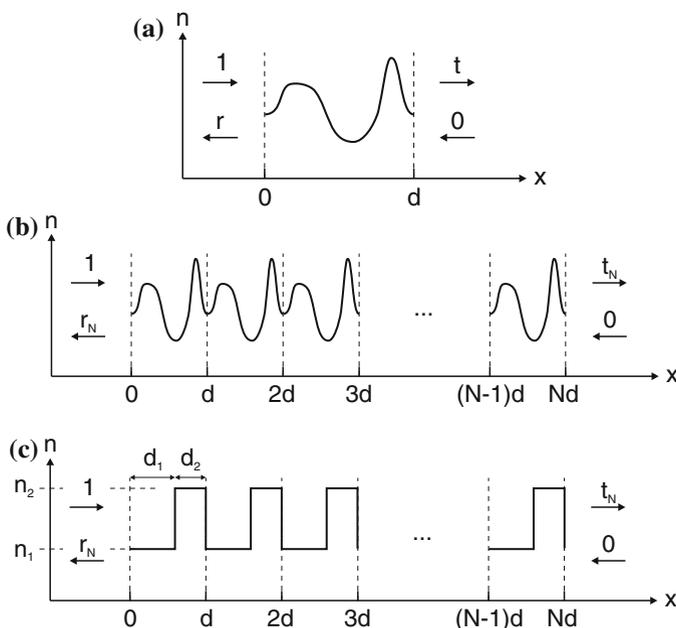

Fig. 19.2 1D scattering problem: (**a**) General scattering of an index of refraction distribution, (**b**) N-period stack, (**c**) two-layer (quarter-wave) stack

where $\tan \phi = y/x$. ϕ is the total phase accumulated during propagation through the structure. It can be written as the product of the physical thickness of the structure d and the effective wave number k. Hence we have the dispersion relation

$$\frac{d}{d\omega} \tan(kd) = \frac{d}{d\omega} \left(\frac{y}{x} \right). \tag{19.7}$$

Evaluating the derivative we find

$$\frac{d}{\cos^2(kd)} \frac{dk}{d\omega} = \frac{y'x - x'y}{x^2}, \tag{19.8}$$

where the prime denotes derivation with respect to ω. Using the relation $\cos^2 \theta = (1 + \tan^2 \theta)^{-1}$, we obtain the general expression

$$\rho(\omega) = \frac{dk}{d\omega} = \frac{1}{d} \frac{y'x - x'y}{x^2 + y^2}. \tag{19.9}$$

19.1.3   Transmission of an N-Period Potential

Now, the behavior of N periods of a given index distribution $n(x)$ within a thickness d of one period (Fig. 19.2b) is investigated. The scattering matrix $\mathbf{M}$ connects the intensity at $x = 0$ with that at $x = d$. We use the column vector $\mathbf{u} = \begin{pmatrix} u^+ \\ u^- \end{pmatrix}$ containing the right- and left-going waves (labeled '+' and '−', respectively), $u^\pm = f^\pm \exp(\pm ikx)$,

$$\mathbf{u}(0) = \mathbf{M}\,\mathbf{u}(d). \tag{19.10}$$

Using the boundary conditions $\mathbf{u}(0) = (1, r)$ and $\mathbf{u}(d) = (t, 0)$, we find that $\mathbf{M}$ has the structure

$$\mathbf{M} = \begin{pmatrix} 1/t & r^*/t^* \\ r/t & 1/t^* \end{pmatrix}. \tag{19.11}$$

The conservation of energy requires that $\det \mathbf{M} = (1 - R)/T = 1$. The eigenvalue equation for $\mathbf{M}$ is

$$\mu^2 - 2\mu \operatorname{Re}(1/t) + 1 = 0. \tag{19.12}$$

The two eigenvalues $\mu^\pm$ are related by $\mu^+ \mu^- = \det \mathbf{M} = 1$. If we consider an infinite, periodic structure, we know from Bloch's theorem that the eigenvector varies between unit cells only via a phase factor, i.e. $|\mu| = 1$. Therefore, the eigenvalues can be written as

$$\mu^\pm = \exp(\pm i\beta), \tag{19.13}$$

where β corresponds to the Bloch phase of a hypothetical infinite periodic structure. This phase β should not be confused with ϕ defined earlier, which is associated with the unit cell transmission. We find the condition

$$\mathrm{Re}(1/t) = \cos\beta \tag{19.14}$$

for the Bloch phase. Since every matrix obeys its own eigenvalue equation, we have also (**1** being the unity matrix)

$$\mathbf{M}^2 - 2\mathbf{M}\cos\beta + \mathbf{1} = 0. \tag{19.15}$$

By induction one can show that the N-period case has the scattering matrix

$$\mathbf{M}^N = \mathbf{M}\frac{\sin(N\beta)}{\sin\beta} - \mathbf{1}\frac{\sin((N-1)\beta)}{\sin\beta}. \tag{19.16}$$

The solution for the finite period case can be written in terms of the Bloch phase of the infinite potential. The transmission and reflection of the N-period system are given by

$$\frac{1}{t_n} = \frac{1}{t}\frac{\sin(N\beta)}{\sin\beta} - \frac{\sin((N-1)\beta)}{\sin\beta} \tag{19.17a}$$

$$\frac{r_n}{t_n} = \frac{r}{t}\frac{\sin(N\beta)}{\sin\beta}. \tag{19.17b}$$

The transmission of intensity can be written as ($T = t^*t$)

$$\frac{1}{T_N} = 1 + \frac{\sin^2(N\beta)}{\sin^2\beta}\left(\frac{1}{T} - 1\right). \tag{19.18}$$

Again, up to this point no specific distribution of the index of refraction within the unit cell has been specified.

From (19.17a), a general formula for the mode density $\rho_N(\omega)$ of the N-stack can be obtained as [1327]

$$\rho_N = \frac{1}{Nd}\frac{\frac{\sin(2N\beta)}{2\sin\beta}\left(\eta' + \frac{\eta\xi\xi'}{1-\xi^2}\right) - \frac{N\eta\xi'}{1-\xi^2}}{\cos^2(N\beta) + \eta^2\left(\frac{\sin(N\beta)}{\sin\beta}\right)^2}, \tag{19.19}$$

where $\xi = x/T = \cos\beta$ and $\eta = y/T$.

19.1.4   The Quarter-Wave Stack

A quarter-wave stack, also known as a Bragg mirror, exhibits a one-dimensional photonic band gap. One period consists of two regions with thickness and index of refraction (d_1, n_1) and (d_2, n_2), respectively (Fig. 19.2c). In the quarter-wave stack each region has an optical thickness of $\lambda/4$ (the wave accumulates in each region a phase of $\pi/2$ for a particular wavelength λ_0 or (midgap) frequency ω_0. Thus, the condition reads

$$n_1 d_1 = n_2 d_2 = \frac{\lambda_0}{4} = \frac{\pi}{2} \frac{c}{\omega_0}. \tag{19.20}$$

Using the Fresnel formulas, the transmission of an arbitrary two-layer cell is

$$t = \frac{T_{12} \, \exp(\mathrm{i}(p+q))}{1 + R_{12} \, \exp(2\mathrm{i}q)}, \tag{19.21}$$

where $p = n_1 d_1 \omega/c$ and $q = n_2 d_2 \omega/c$ are the phases accumulated in the two layers, respectively. The values of T_{12} and R_{12} are given as

$$T_{12} = \frac{4 \, n_1 \, n_2}{(n_1 + n_2)^2} \tag{19.22a}$$

$$R_{12} = \frac{(n_1 - n_2)^2}{(n_1 + n_2)^2} \,. \tag{19.22b}$$

For the quarter-wave stack ($p = q = \pi/2$), we obtain for (19.21)

$$t = \frac{T_{12} \, \exp(\mathrm{i}\pi\tilde{\omega})}{1 + R_{12} \, \exp(\mathrm{i}\pi\tilde{\omega})}, \tag{19.23}$$

where $\tilde{\omega} = \omega/\omega_0$ is the frequency scaled to the midgap value.
    The transmission of a single two-layer cell is

$$T = \frac{T_{12}^2}{1 - 2 \, R_{12} \, \cos(\pi\tilde{\omega}) + R_{12}^2}, \tag{19.24}$$

and the Bloch phase is given by

$$\cos\beta = \xi = \frac{\cos(\pi\tilde{\omega}) - R_{12}}{T_{12}} \tag{19.25a}$$

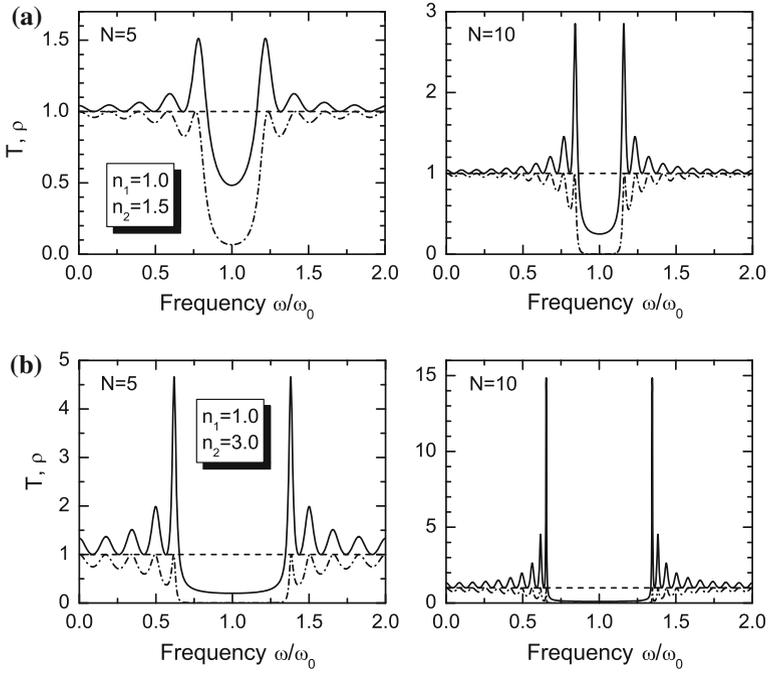$$\eta = \frac{\sin(\pi\tilde{\omega})}{T_{12}} \,. \tag{19.25b}$$

Fig. 19.3 Quarter-wave stack with indices of refraction (**a**) n_1, n_2 = 1.0, 1.5 and (**b**) 1.0, 3.0. *Solid lines* dimensionless density of modes ρ_N (19.19), *dashed lines* transmission T_N (19.26) for two different numbers of pairs $N = 5$ (*left panels*) and 10 (*right panels*) versus the dimensionless frequency $\tilde{\omega}$

For the N-period quarter-wave stack the transmission is given by

$$T_N = \frac{1 + \cos \beta}{1 + \cos \beta + 2 \left(R_{12}/T_{12}\right) \sin^2(N \beta)}. \tag{19.26}$$

A band gap forms. Within the band gap, the density of modes is lowered, at the edges it is enhanced (Figs. 19.3 and 19.4). The transmission at midgap decreases $\propto \left(n_i/n_j\right)^{2N}$, where $n_i < n_j$.

In the limit of large N the complete width $\Delta\tilde{\omega}$ of the band gap is implicitly given by

$$\cos \left(\frac{\pi}{2} \Delta\tilde{\omega}\right) = 1 - 2 \left(\frac{n_1 - n_2}{n_1 + n_2}\right)^2. \tag{19.27}$$

If $|n_1 - n_2| \ll n_1 + n_2$, we find

$$\Delta\tilde{\omega} \approx \frac{4}{\pi} \frac{|n_1 - n_2|}{n_1 + n_2}. \tag{19.28}$$
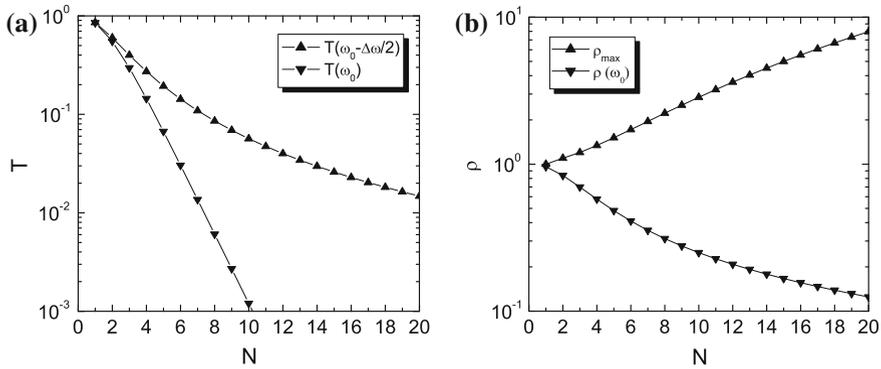
Fig. 19.4 Quarter-wave stack with indices of refraction n_1, n_2 = 1.0, 1.5: (**a**) Transmission T_N at midgap ($\tilde{\omega} = 1$, *down triangles*) and at the band edge ($\tilde{\omega} = 1 - \Delta\tilde{\omega}/2$, *up triangles*) versus number of pairs N. (**b**) Dimensionless density of modes ρ_N at maximum near the band edge and at midgap versus number of pairs N

The principle of the quarter-wave stack is scalable to frequencies other than visible light.[1] In Fig. 19.5 the reflectance of various quarter-wave stacks from yttria-stabilized zirconia (YSZ [1328], high index material, Fig. 19.6a) and Al_2O_3 are shown [1329]. The different design wavelengths have been achieved solely by varying the layer thicknesses.

In Fig. 19.6b the three Bragg mirrors from Fig. 19.5 with $N = 15.5$ pairs are replotted in relative frequency units $\tilde{\omega}$. The spectra look very similar; subtle differences in the width of the reflectance band are due to slightly larger index contrast at higher design energy (cmp. Fig. 19.6a). The width of the gap is approximately $\Delta\tilde{\omega} \approx 0.18$ in agreement with (19.28).

As further example, a Mo/Si Bragg mirror with a period of 6.7 nm is shown in Fig. 19.7. Such a mirror works in the extreme UV and is used for soft X-ray optics, possibly in advanced lithography systems. Dielectric thin films can also be designed for anti-reflection coatings, edge filters or pass and stop band filters as detailed in [1326].

19.1.5   Formation of a 3D Band Structure

For other applications, e.g. waveguides with minimized footprint, 3D (or at least 2D) photonic band gap structures are needed. Details can be found in dedicated textbooks [1332–1334]. In [1335] planar, cylindrical and spherical Bragg mirrors are discussed.

---

[1]This is a general property of Maxwell's equations which do not contain a specific length scale.
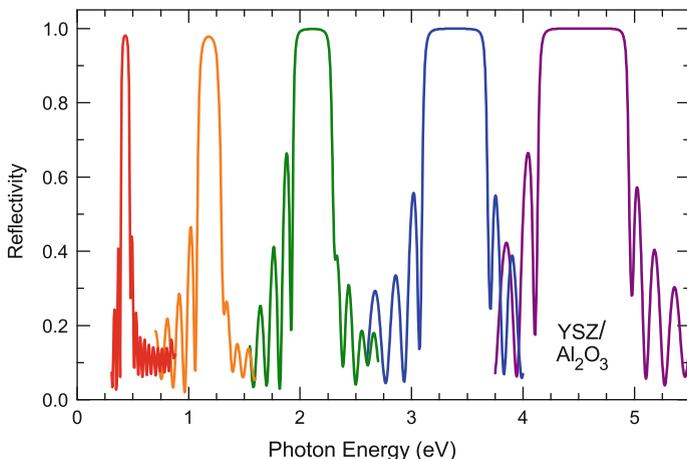
Fig. 19.5 Reflectance of various Bragg mirrors from YSZ/Al₂O₃ grown by pulsed laser deposition on sapphire. The different layer thicknesses result in the design energies 0.43 eV ($N = 10.5$, $R_{max} = 0.9812$, *red*), 1.19 eV ($N = 10.5$, $R_{max} = 0.9779$, *orange*), 2.11 eV ($N = 15.5$, $R_{max} = 0.99953$, *green*), 3.39 eV ($N = 15.5$, $R_{max} = 0.99946$, *blue*) and 4.54 eV ($N = 15.5$, $R_{max} = 0.99989$, *purple*)
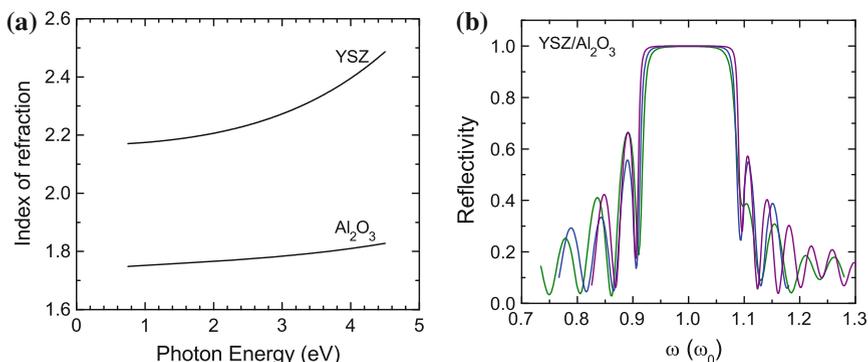

Fig. 19.6 (**a**) Index of refraction of YSZ and Al₂O₃ as a function of photon energy. (**b**) Reflectance spectra of the 2.11 eV, 3.39 eV and 4.54 eV Bragg mirrors of Fig. 19.5 replotted as a function of the scaled frequency $\tilde{\omega} = \omega/\omega_0$

Since we want a photonic band gap that is present for *all* directions of propagation, a Brillouin zone with a shape close to a sphere is preferable. Then, the main directions are at similar k-values (Fig. 19.8). One of the best suited is the fcc lattice. Since the L point is centered at $\approx 14\%$ lower frequency than the X point, the forbidden gaps for different directions must be, however, sufficiently wide to create a forbidden frequency band overlapping at all points along the surface of the Brillouin zone. For example, the bcc lattice has a Brillouin zone that is less symmetric than that of the fcc lattice (see Fig. 3.34) and thus is less suited for the creation of an omnidirectional
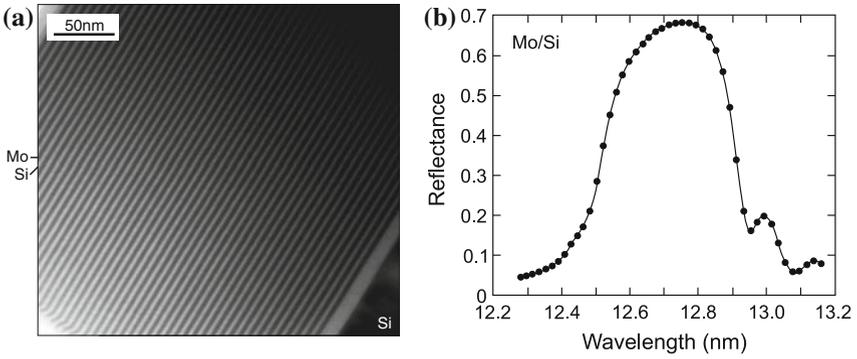
Fig. 19.7 (**a**) Cross-sectional TEM of Mo/Si superlattice with 2.7 nm Mo and 4.0 nm Si (period: 6.7 nm) on Si(001) substrate. From [1330]. (**b**) Reflection spectrum for a SL with period of 6.5 nm and 88.5° angle of incidence. Data points are shown as *circles*, the *solid line* is a fit with a period of 6.45 nm. Adapted from [1331]
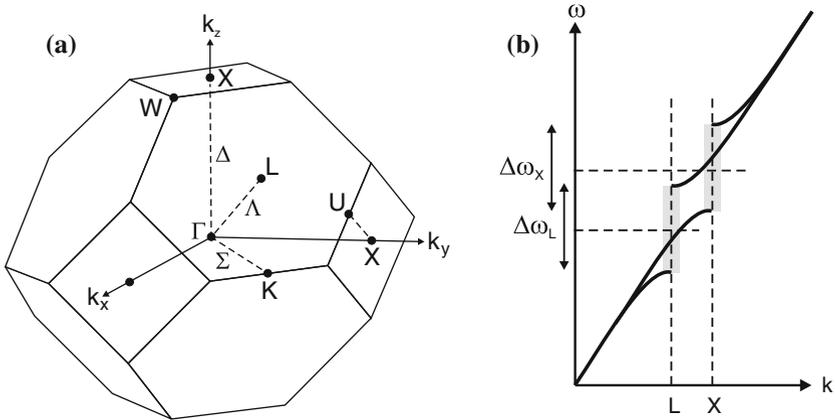

Fig. 19.8 (**a**) The Brillouin zone of the fcc lattice. (**b**) Schematic forbidden gaps at the L and X points

photonic band gap. However, the photonic band gap must not arise above the first band, relaxing problems due to asymmetry of the Brillouin zone (cf. Table 19.1).

Maxwell's equations (zero charge density) for monochromatic waves $\propto \exp(\mathrm{i}\omega t)$

$$\nabla \cdot \mathbf{D} = 0 \tag{19.29a}$$

$$\nabla \times \mathbf{E} = \mathrm{i}\,\frac{\mu\,\omega}{c}\mathbf{H} \tag{19.29b}$$

$$\nabla \times \mathbf{H} = \mathrm{i}\,\frac{\omega}{c}\mathbf{D} \tag{19.29c}$$

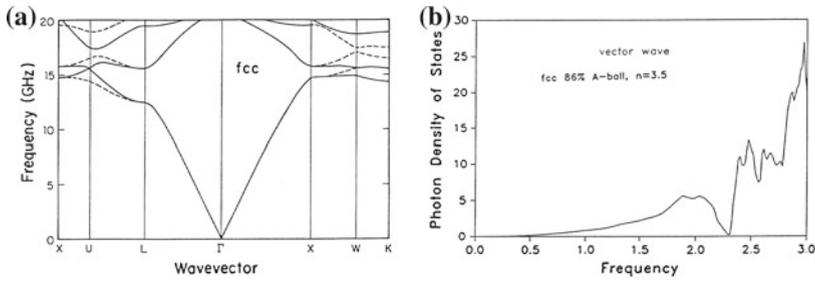$$\nabla(\mu\mathbf{H}) = 0\,, \tag{19.29d}$$

Fig. 19.9 (**a**) Calculated photonic band gap structure of a fcc dielectric structure composed of air spheres in a dielectric background of refractive index $n = 3.5$. The filling ratio is 86 % air and 14 % dielectric material. *Dotted* and *solid lines* represent coupling to s- and p-polarized light, respectively. Reprinted with permission from [1336], ©1990 APS. (**b**) Density of states for the band structure of part (**a**)
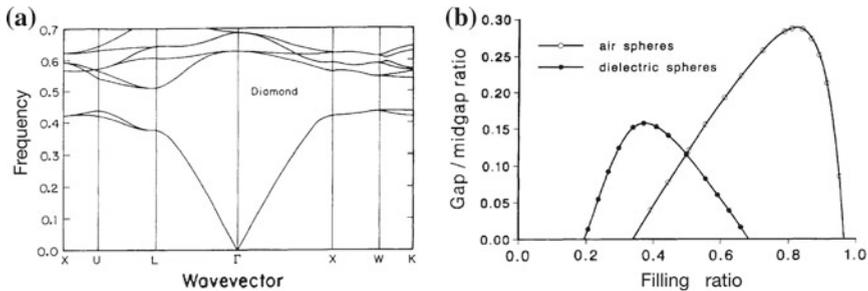

Fig. 19.10 (**a**) Calculated photonic band structure for a diamond dielectric structure consisting of overlapping air spheres in a dielectric material with $n = 3.6$. Filling ratio of air is 81 %. The frequency is given in units of c/a, a being the cubic lattice constant of the diamond lattice and c being the velocity of light. (**b**) Gap-to-midgap frequency ratio for the diamond structure as a function of filling ratio for dielectric spheres $n = 3.6$ in air (*solid circles*) and air spheres in dielectric n. Optimal case: air spheres with 82 % filling ratio. Reprinted with permission from [1336], ©1990 APS

together with $\mathbf{D}(\mathbf{r}) = \epsilon(\mathbf{r})\mathbf{E}(\mathbf{r})$ and $\mu = 1$ they are combined into the wave equation

$$\nabla \times \left[\epsilon^{-1}(\mathbf{r}) \nabla \times \mathbf{H}(\mathbf{r})\right] + \frac{\omega^2}{c^2} \mathbf{H}(\mathbf{r}) = 0. \qquad (19.30)$$

This equation is numerically solved for planar waves with wavevector $\mathbf{k}$.

In the following, results are shown for various structures. In a fcc lattice of air spheres in a dielectric medium with $n = 3.6$ (a typical semiconductor), no band gap can be achieved (Fig. 19.9a), only a pseudogap (Fig. 19.9b) appears.

In a diamond lattice (two fcc lattices shifted by $1/4 \langle 111 \rangle$), a complete photonic band gap is possible [1336] (Fig. 19.10). Recently, a periodic array of spirals (Fig. 19.11) has been predicted to exhibit a large photonic band gap [1337]. Glancing-angle deposition [1338] (GLAD) is a way to realize such structures. Another method
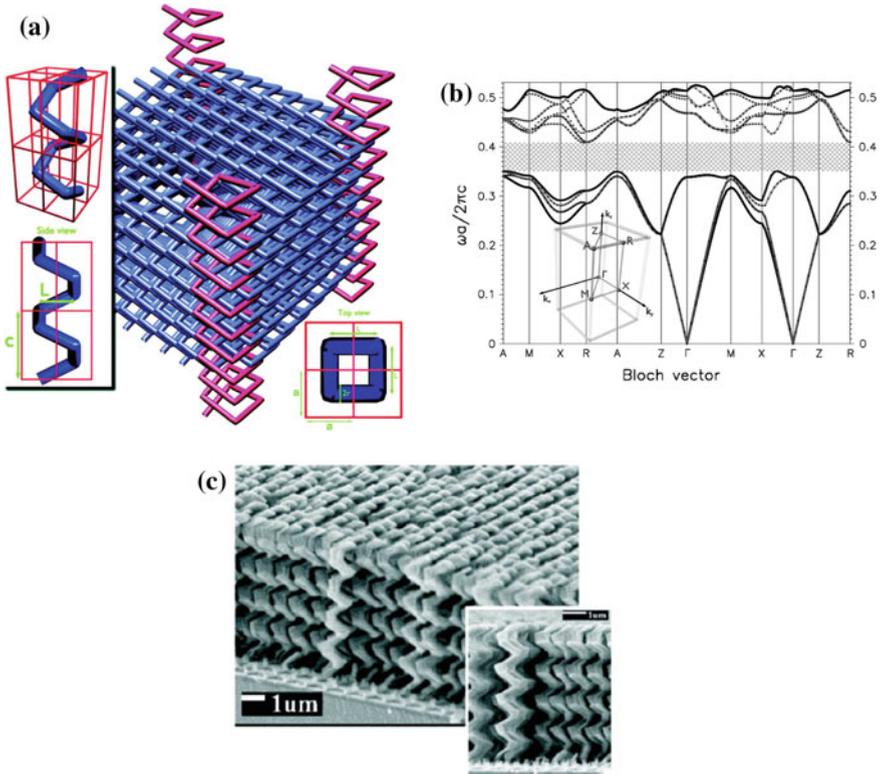
Fig. 19.11 (**a**) Tetragonal square-spiral photonic crystal. The crystal shown here has a solid filling fraction of 30 %. For clarity, spirals at the corners of the crystal are highlighted with a different shade and height. The tetragonal lattice is characterized by lattice constants a and b. The geometry of the square spiral is illustrated in the insets and is characterized by its width, L, cylinder radius, r, and pitch, c. The *top left inset* shows a single spiral coiling around four unit cells. (**b**) Band structure for the direct structure crystal characterized by $[L, C, r]$=[1.6, 1.2, 0.14] and a spiral filling factor $f_{spiral} = 30$ %. The lengths are given in units of a, the lattice constant. The width of the PBG is 15.2 % relative to the center frequency for background dielectric constant $\epsilon_b = 1$ and spiral dielectric constant $\epsilon_s = 11.9$. The positions of high-symmetry points are illustrated in the *inset*. Reprinted with permission from [1337], ©2001 AAAS. (**c**) Oblique and edge views of a tetragonal square spiral structure grown using the GLAD (glancing-angle deposition) process. Reprinted with permission from [1338], ©2002 ACS

to fabricate structures with arbitrary geometry within a material is two-photon lithography or two-photon holography. Another path to PBG structures are so-called inverted opals. First, a close-packed structure of spheres, e.g. monodisperse silica spheres, is fabricated by sedimentation or self-assembly. The gaps are filled with a high-index medium and the template is subsequently removed, e.g. by etching or dissolving. The resulting structure is shown in Fig. 19.12a. Such a structure has a photonic band gap (Fig. 19.12b) if the refractive index is sufficiently high (>2.85) [1339].
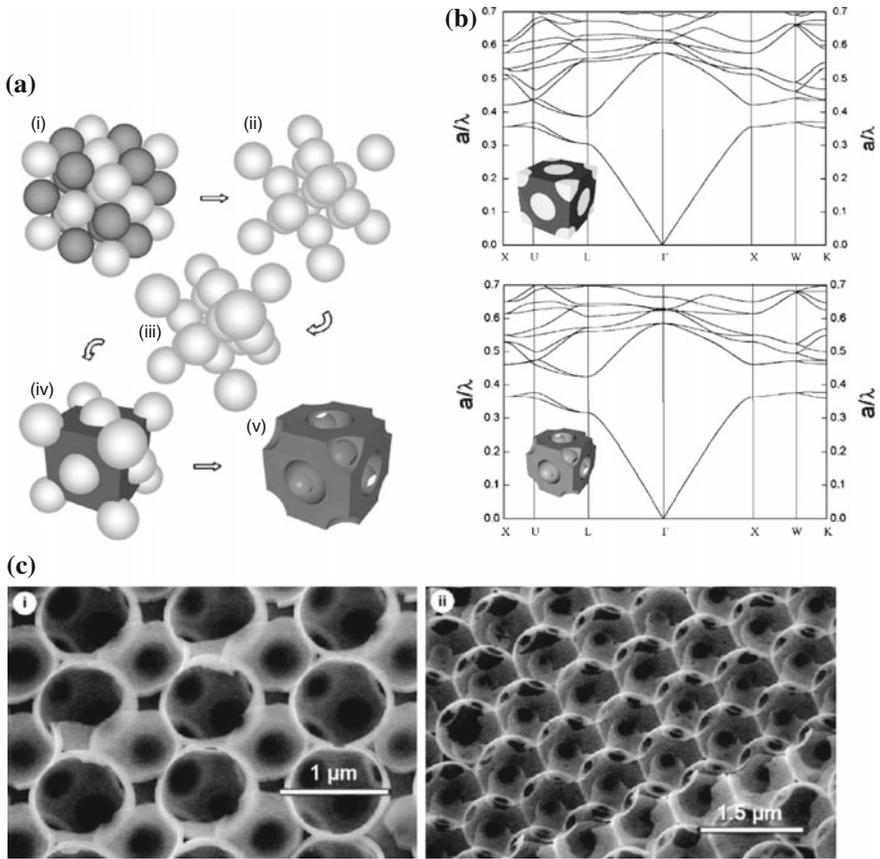
Fig. 19.12 (**a**) Cartoon showing, in five steps, the fabrication of an inverse diamond structure with a full photonic band gap. First, (i) a mixed body-centered cubic lattice is assembled (ii) after which the latex sublattice is removed; (iii) then the structure is sintered to a filling fraction of ~50% after that (iv) silicon or germanium infiltration takes place and finally (v) silica elimination. (**b**) Photonic band diagrams of (upper panel) a silicon/silica composite diamond opal and (lower panel) made of air spheres in silicon resulting from the removal of the silica spheres from the former. The filling fraction for silicon is 50%. The inset shows the corresponding real space structures. Reprinted with permission from [1347], ©2001 AIP. (**c**) SEM images of internal facets of silicon inverse opal: (i) (110) facet, (ii) (111) facet. Adapted from [1348], reprinted with permission from Nature, ©2000 Macmillan Magazines Limited

The band gap in this case is between the 4th and 5th band. Table 19.1 offers a compilation of various PBG structures and their properties.

Table 19.1 Various photonic band gap structures and some of their properties

Name	Crystal type	n	$\Delta\tilde{\omega}$ (%)	Reference
Diamond	Diamond	2	29	[1336]
Yablonovite	fcc	2	19	[1340]
Woodpile	fc tetragonal	2	20	[1341]
Spirals	sc	4	17	[1342]
Square-spirals	Tetragonal	4	24	[1337]
Layered 3D	bc orthorhombic	4	23	[1343]
Inverted scaffold	sc	5	7	[1344]
Inverse opal	fcc	8	4.25	[1345]
Inverse hcp	hcp	16	2.8	[1346]

The band gap is between the nth and $(n+1)$th band, $\Delta\tilde{\omega}$ is given for air/silicon ($\epsilon \approx 12$)

19.1.6   Disorder

A real photonic band gap structure deviates from the ideal, perfectly periodic system by slight variations of the position and possibly also the size of the dielectric 'atoms'. This is schematically shown in Fig. 19.13a. The difference between the real and ideal structure is a (bipolar) spatial distribution of $\Delta\epsilon(\mathbf{r})$ which acts as a source of scattering and hence exponential attenuation of coherent beams propagating through photonic crystals over lengths l, named the '(extinction) mean free path'. After propagating over such distance l, a light beam is converted to a diffuse glow that corrupts the functionality of any photonic integrated circuit. Experimentally for opals a mean free path consistent with 5 % fabrication accuracy has been found (Fig. 19.13b). For such disorder and a lattice constant $a \approx \lambda$, the mean free path is about only 10 wavelengths, $l \approx 10\lambda$.

19.1.7   Defect Modes

Similar to a perfect periodic atomic arrangement leading to the formation of the electronic band structure, a perfectly periodic dielectric structure leads to the photonic band structure. As we know from semiconductor physics, much of the interesting physics and numerous applications lie in defect modes, i.e. localized electronic states due to doping and recombination at such centers. The equivalent in PBG structures are point defects (one unit missing) or line defects (a line of units, straight, bend or with sharp angles, missing). Such defects create localized states, i.e. regions for light localization. In the case of line defects we deal with waveguides that can be conveniently designed and could help to reduce the size of photonic and optoelectronic integrated circuits.
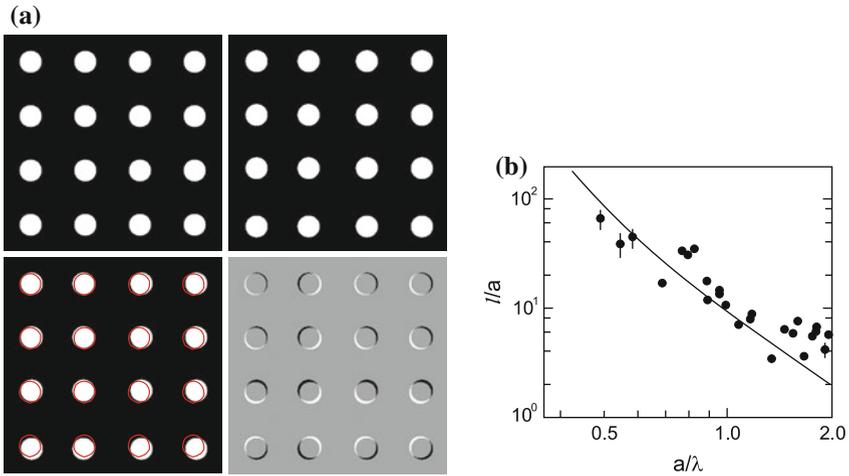
(a)

(b)

Fig. 19.13 (**a**) Schematic photonic band gap structure with perfect (*upper left*) and disordered (*upper right*) periodicity. In the *lower left* panel the disordered structure is overlayed with the ideal structure (*red circles*). In the *lower right* panel, the difference between ideal and disordered structure is shown. (**b**) Optical mean free path in an opal photonic band gap structure for various lattice constants. *Solid line* is theory for 5 % fabrication accuracy. Adapted from [1349]

1D Model

We revisit our 1D scattering theory and create now a 'defect'. A simple defect is the change of the width of the center n_2-region in a quarter-wave stack. For the numerical example, we choose $N = 11$, $n_1 = 1$, $n_2 = 2$.

In Fig. 19.14, the transmission curves are shown for the undisturbed quarter-wave stack and the microcavity with $n_2 d_2^{\text{center}} = 2\lambda_0/4 = \lambda_0/2$. A highly transmissive mode at $\omega = \omega_0$ arises that is quite sharp with $\Delta\omega = 3 \times 10^{-4}$. Thus, the quality factor Q, also called the Q-factor or finesse,

$$Q = \frac{\omega_0}{\Delta\omega}, \tag{19.31}$$

with ω_0 being the resonance frequency and $\Delta\omega$ being the linewidth, is 3.3×10^3 in this case.

If the thickness is varied (Fig. 19.15), the mode shifts away from the center. A similar scenario arises for higher-order $n_l/2$-cavities, e.g. $n_2 d_2^{\text{center}} = 4\lambda_0/4 = \lambda_0$ (Fig. 19.16).
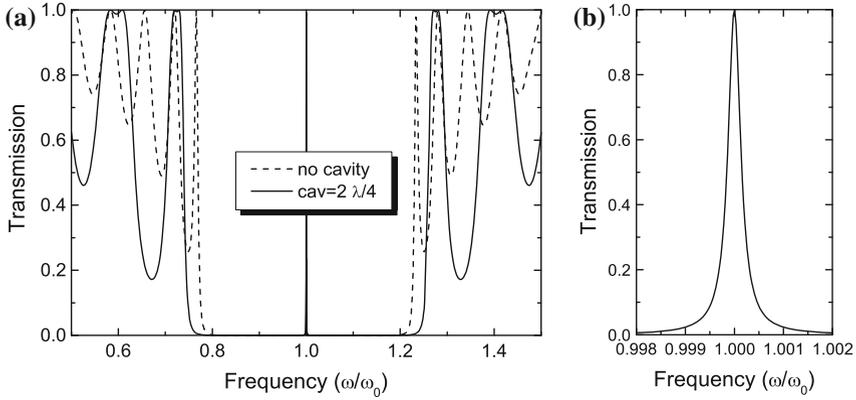
Fig. 19.14 Defect mode in 1D photonic band gap: (**a**) Transmission of $N = 11$ quarter-wave stack exhibiting a photonic band gap ($n_1 = 1$, $n_2 = 2$) (*dashed line*) and of microcavity (*solid line*) with center n_2-region of width $\lambda_0/2$ (instead of $\lambda_0/4$). (**b**) Relative width of mode is about 3×10^{-4}

Fig. 19.15 Transmission of $N = 11$ quarter-wave stack ($n_1 = 1$, $n_2 = 2$) with center n_2-region of widths $1.8\,\lambda_0/4$ (*dashed line*) and $2.2\,\lambda_0/4$ (*solid line*)
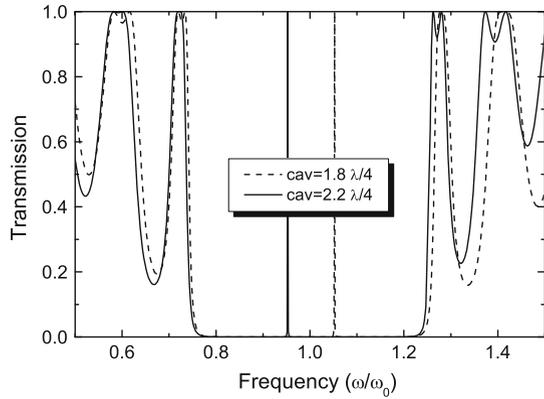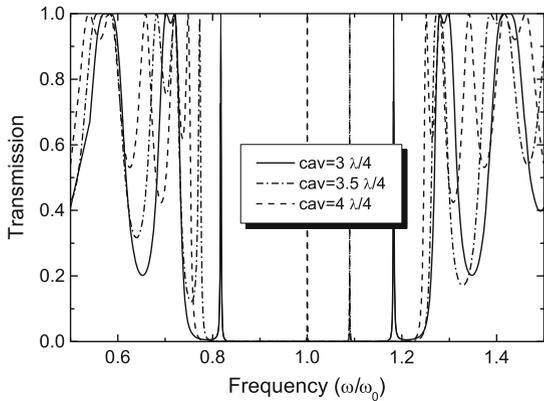

Fig. 19.16 Transmission of $N = 11$ quarter-wave stack ($n_1 = 1$, $n_2 = 2$) with center n_2-regions of widths $3\,\lambda_0/4$ (*solid line*), $3.5\,\lambda_0/4$ (*dash-dotted line*) and $4\,\lambda_0/4$ (*dashed line*)

2D or 3D Defect Modes

An example of 2D waveguiding is shown in Fig. 19.17. Point defects can be used
for high-finesse wavelength filtering. Emitters surrounded by a photonic band gap
material with a defect mode can emit into the defect mode only, leading to spectrally
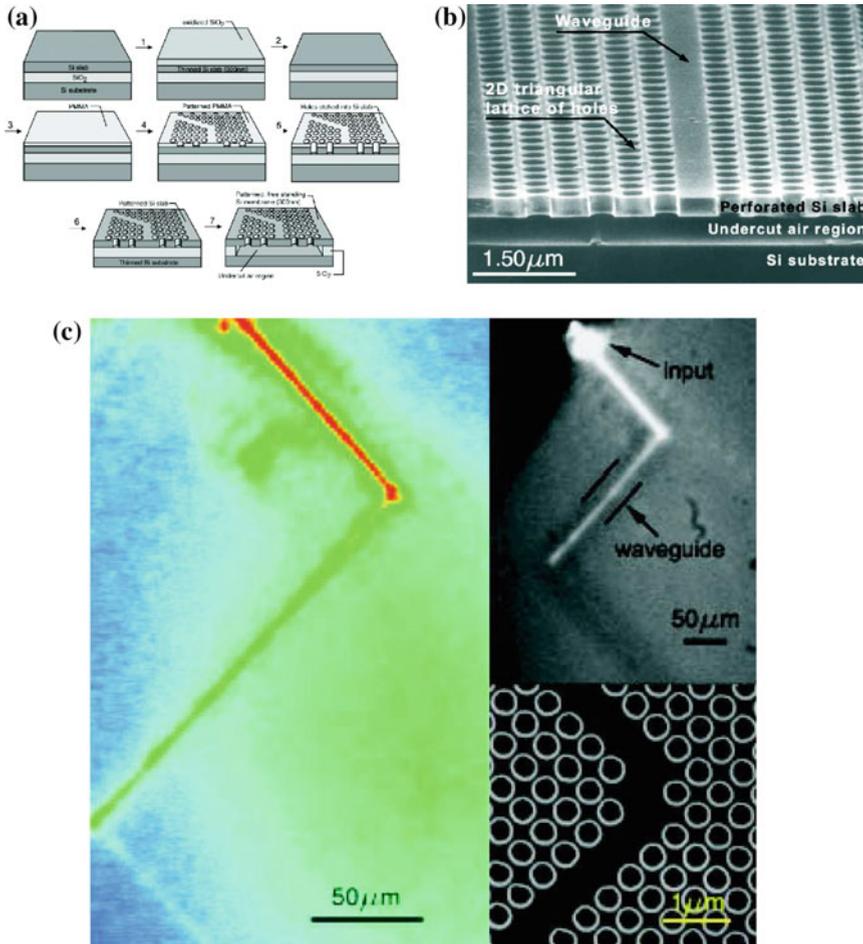filtered, highly directional emission.

Fig. 19.17   2D photonic band gap waveguide structure. (**a**) Fabrication principle, (**b**) SEM image
of the structure, (**c**) light guiding at a 90° bend. Reprinted with permission from [1350], ©2000 AIP

19.1.8   Coupling to an Electronic Resonance

In a vertical-cavity surface-emitting laser (cf. Sect. 23.4.14), an optical defect mode
in a 1D dielectric structure is coupled to an electronic excitation, such as an exciton
in a quantum well or dot. In the simplest picture, the oscillator must emit its radiation
into the cavity mode since other modes do not exist in the Bragg band. Thus, the
emission energy is given and fixed by the cavity mode. However, the photon mode
(field oscillator) and the electronic oscillator form a coupled system that generally
must be described using quantum electrodynamics. Energy is periodically exchanged
between the two oscillators with the Rabi frequency. An analogous phenomenon is
investigated in the field of atom–cavity interactions. A necessary condition for the
observation of such an oscillation is that the radiation energy remains long enough
in the cavity that can be expressed as [1351, 1352] (cf. (19.37))

$$\alpha\, d \gg 1 - R \approx \pi/Q, \tag{19.32}$$

where α is the absorption coefficient of the electronic transition, d is the length of
the absorbing medium, R is the reflectance of the cavity mirror and Q is the finesse
of the cavity given in (19.31). This situation is called the *strong coupling* regime
since it leads to anticrossing behavior of the cavity mode and electronic resonance.
In the *weak coupling* regime for small absorption, the resonances cross (within their
linewidth). For resonance, the emission intensity of the oscillator into the cavity
mode is enhanced and its lifetime is reduced (Purcell effect), which is discussed in
Sect. 19.2.2.

The transmission T of a Fabry–Perot cavity with two (equal and lossless) mirrors
of transmission $T_m = 1 - R_m$ is given by

$$T(\omega) = \frac{T_m^2 \exp\left(-2\,L\,\alpha(\omega)\right)}{\left|1 - R_m \exp\left(\mathrm{i}\,2\,n^*\,L\,\omega/c\right)\right|^2}, \tag{19.33}$$

with the complex index of refraction $n^* = n_r + \mathrm{i}\kappa = \sqrt{\epsilon}$ and $\alpha = 2\omega\kappa/c$ (cf. (9.9)).
For an empty cavity, i.e. a (small) background absorption α_B and a background
index of refraction $n_r = n_B$, the resonances occur when the phase shift $2n_B L\omega/c$ is
an integer multiple of 2π, i.e. for

$$\omega_m = m\,\frac{\pi\,c}{n_B\,L}, \tag{19.34}$$

with $m \geq 1$ being a natural number. In the vicinity of the resonance, i.e. for $\omega = \omega_m + \delta\omega$, we can expand $\exp\left(2n_B L\omega/c\right) \approx 1 + \mathrm{i}2n_B L\delta\omega/c$ and obtain from (19.33)
a Lorentzian for the transmission

$$T(\omega) \approx \frac{T_m^2 \exp\left(-2L\alpha(\omega)\right)}{\left|1 - R_m(1 + \mathrm{i}2n_B L\,\delta\omega/c)\right|^2} = \frac{(T_m/R_m)^2 \exp\left(2L\alpha(\omega)\right)}{(\delta\omega)^2 + \gamma_c^2}. \tag{19.35}$$

The frequency width (HWHM) γ_c of the empty-cavity resonance is given by

$$\gamma_c = \frac{1 - R'}{R'} \frac{c}{2 n_B L},$$ (19.36)

where $R' = R_m \exp(-2L\alpha)$. Thus, the decay rate (photon loss from the cavity) is proportional to $T_m + \alpha_B L$ if both terms are small. The quality factor of the cavity resonance m is given by

$$Q = \frac{\omega_m}{2\gamma_c} \approx \frac{m\pi}{1 - R}.$$ (19.37)

Now, the electronic resonance is put into the cavity leading to a change in the dielectric function to (cf. (D.11))

$$\epsilon = n_B^2 \left[1 + \frac{f}{1 - (\omega^2 + i\omega\Gamma)/\omega_0^2} \right],$$ (19.38)

where the index of refraction due to the electronic resonance is given by $n(\omega) = \sqrt{\epsilon}$ and (D.13a, b). For resonance of the cavity mode and the electronic oscillator, i.e. $\omega_m = \omega_0$, the solution for the cavity resonance condition $2n_r\omega L/c = m2\pi$ is obtained, using (19.34), from

$$n_r(\omega) = m\frac{\pi c}{\omega L} = n_B \frac{\omega_m}{\omega}.$$ (19.39)

A graphical solution (Fig. 19.18a) yields three intersections of the left and right hands of (19.39). The very high absorption at the central solution ($\omega = \omega_0$) results in very low transmission. The other two solutions[2] yield the frequencies of the coupled normal mode peaks. For $f \ll 1$, we use (D.13a) in (19.39) and find for the splitting $\pm\Omega_0/2$ of the two modes

$$\Omega_0^2 = f\omega_0^2 - \Gamma^2.$$ (19.40)

This frequency is called the Rabi frequency. If the dielectric function of the oscillator is put into (19.33), the splitting is found to be

$$\Omega_0^2 = f\omega_0^2 - (\Gamma - \gamma_c)^2.$$ (19.41)

A splitting will only be observable if $\Omega_0 \gg \Gamma, \gamma_c$. If the two resonances ω_c and ω_0 are detuned by $\Delta = \omega_c - \omega_0$, the splitting Ω of the transmission peaks shows the typical anticrossing behavior of two coupled oscillators

$$\Omega^2 = \Omega_0^2 + \Delta^2.$$ (19.42)

---

[2]These solutions only occur for sufficient oscillator strength $f > (\Gamma/\omega_0)^2$, i.e. in the strong coupling regime where $\Omega_0^2 > 0$. The absorption coefficient at ω_0 must be larger than $\Gamma n_\infty/c$.
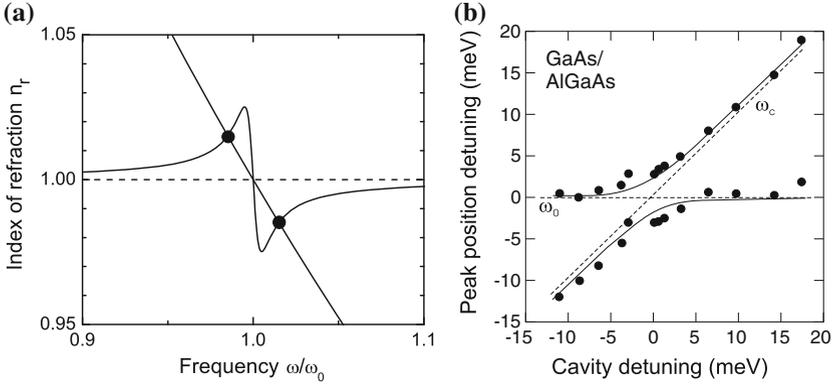
(a)

(b)

Fig. 19.18 (**a**) Graphical representation of (19.39) with the two solutions marked with *circles* for $n_\infty = 1$ (*dashed line*), $f = 10^{-3}$, $\Gamma/\omega_0 = 10^{-2}$ and $\omega_0 = \omega_\mathrm{m}$. (**b**) Reflectance peak positions (experimental data (*circles*) at $T = 5\,\mathrm{K}$) versus cavity detuning $\omega_\mathrm{c} - \omega_0$ for a cavity with two GaAs/AlGaAs Bragg mirrors (24/33 pairs for the front/bottom mirror) and five embedded quantum wells whose resonances are closely matched. *Solid lines* are a theoretical fit according to (19.42) with $\Omega_0 = 4.3\,\mathrm{meV}$. The *dashed lines* show the electronic resonance ω_0 and the cavity resonance ω_c. Part (**b**) adapted from [1352]

In the experiment, typically the electronic resonance remains fixed at ω_0 and the cavity resonance is detuned by variation of the cavity length across the wafer (Fig. 19.18b).

A detailed theory of cavity polaritons is given in [1353]. The nonlinear optics of normal mode coupling in semiconductor microcavities is reviewed in [1354].

The in-plane dispersion of the cavity polaritons depends on the coupling strength. First, the photon dispersion is given by

$$E_\mathrm{ph}(\mathbf{k}) = \hbar\omega = \hbar c\, k = \hbar c \left(k_\parallel^2 + k_z^2\right)^{1/2}, \tag{19.43}$$

where $k_\parallel$ is the in-plane k-vector and k_z is given by the resonance condition, $k_z = \omega_m/c$ with (19.34),

$$k_z = m\,\frac{\pi}{n_\mathrm{B}\, L}. \tag{19.44}$$

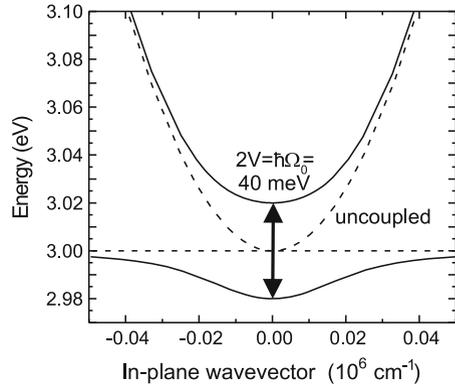Thus the dispersion relation is no longer linear as for freely propagating light.

For small $k_\parallel$ this leads to an (in-plane) effective photon 'rest mass', applying (6.34),

$$\frac{1}{m_\mathrm{ph}^*} = \frac{1}{\hbar^2}\,\frac{\partial^2 E_\mathrm{ph}}{\partial k^2}. \tag{19.45}$$

We find

$$m_\mathrm{ph}^* = \frac{\hbar k_z}{c} = \frac{\hbar\,\omega(k_\parallel = 0)}{c^2}. \tag{19.46}$$

Fig. 19.19 Dispersion of cavity photon mode and electronic resonance at $E_{el} = 3.0\,\text{eV}$ (*dashed lines*) and coupled modes (*solid lines*) for $2V = 40\,\text{meV}$

Now we assume the electronic oscillator to be in resonance with the photon dispersion at $k_\parallel = 0$, i.e. $E_{el} = \hbar\omega(k_\parallel = 0)$. The electronic resonance shall have vanishing dispersion for simplicity since the exciton mass is much larger than (19.46). The eigenwert equation of the coupled system, resembling (6.57), is

$$\begin{vmatrix} E - E_{ph} & V \\ V & E - E_{el} \end{vmatrix} = 0, \tag{19.47}$$

with two solutions, called the upper and lower cavity polariton branch, visualized in Fig. 19.19. Their splitting at $k_\parallel = 0$ is $2V$. Thus the coupling parameter $V = \hbar\Omega_0/2$ corresponds [1353] to the Rabi frequency (19.40). Experimental values for the splitting of 3–15 meV in InAlGaAs based [1352, 1355–1358], 17–44 meV in CdZnTeSe based [1359], 6–60 meV in (Al,In,Ga)N based [1360–1364] and 78 meV in ZnO based [1365] microcavities were found. It is possible to condensate cavity polaritons in the minimum of the dispersion around $k_\parallel = 0$ (Bose–Einstein condensation). In [1366] stimulated scattering and gain from cavity polaritons have been reported. Further details on cavity polaritons can be found in [1367, 1368].

19.2 Microscopic Resonators

19.2.1 Microdiscs

A microdisc is a cylindrical resonator with a thickness d that is small compared to the radius R. It can be fabricated from semiconductors and semiconductor heterostructures using patterning and material-selective etching. With underetching a mostly free-standing disc can be made that resides on a post (Fig. 19.20).

The coordinate system is (ρ, ϕ, z) with the z direction being perpendicular to the disc area. Typically, the disc is so thin that there is only one node along z. Solving the
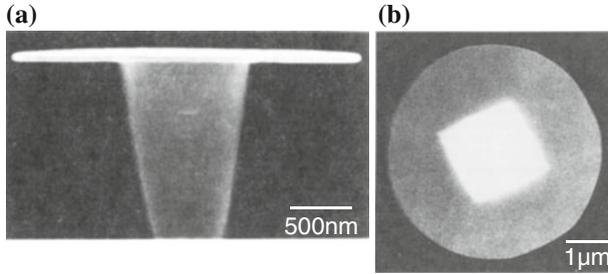
(a)   **(b)**

Fig. 19.20 (**a**) Side view of a 3-μm diameter disc containing one 10-nm InGaAs quantum well between 20-nm InGaAsP barriers standing on an InP pillar that has been selectively underetched using HCl. (**b**) Top view SEM image of a 5-μm diameter InGaAsP microdisc. The pedestal shape is a rhombus due to anisotropic etching of the HCl. Adapted from [1369], reprinted with permission, ©1992 AIP
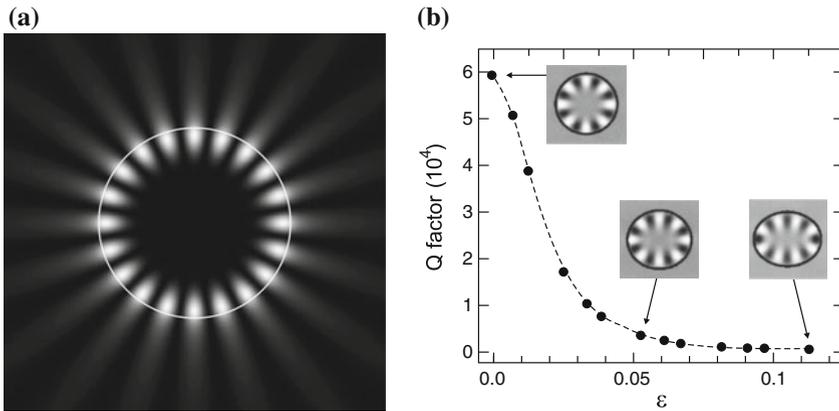
(a)   **(b)**

Fig. 19.21 (**a**) Field intensity for whispering gallery mode (10, 0) (TM-polarized) for a circle with 1 μm radius (shown as *white line*) and $n = 1.5$. The image size is $4 \times 4 \, \mu m^2$. (**b**) Theoretical quality factor of a 2-μm InP microdisc as a function of the deformation parameter (19.49). The *insets* show (8,0) whispering gallery modes at a wavelength of 1.55 μm for $n = 3.4$. Part (**b**) adapted from [1372]

wave equation in this geometry [1370], the modes are characterized by two numbers (m, l). m describes the number of zeros along the azimuthal direction ϕ with the field amplitude being proportional to $\exp(\pm i m \phi)$. Thus, except for $m = 0$, the modes are simply degenerate. Modes with $E_z = 0$ are called TE modes. This is the preferred polarization of emission. The number l denotes the number of zeros in the radial direction. Only for modes with $|m| = 1$, is the intensity nonzero on the axis, i.e. for $\rho = 0$. All other modes have vanishing intensity in the disc center.

The light intensity in whispering gallery modes is preferentially concentrated along the circumference of the disc as shown in Fig. 19.21a. Since the light can only escape via evanescent waves, the light is well 'captured' in such a mode.
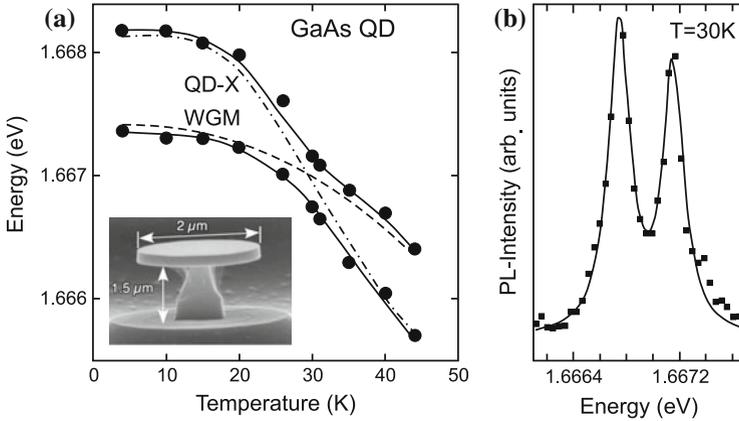
Fig. 19.22 Strong coupling of a single QD exciton (due to monolayer fluctuation in a 13 ML thick GaAs/Al$_{0.33}$Ga$_{0.67}$As QW) with a WGM in a microdisk of 2 μm diameter (*inset*). (**a**) Anti-crossing of upper and lower peak for various temperatures. *Symbols* are data points, *solid lines* are theory considering coupling. The *dashed* (*dash-dotted line*) is the expected temperature shift of the WGM mode (exciton energy). (**b**) Photoluminescence spectrum at the anti-crossing point ($T = 30$ K). Experimental data (*squares*) and fit with two peaks (*solid line*). Adapted from [1373]

The *Q*-factor (19.31) is extremely high and takes values of several 10^4. In order to couple light out of such a disc, deformed resonators, e.g. with a defect in the form of protrusions [1371], were devised. Deformed resonators are discussed in more detail in the next section.

The strong coupling of a QD exciton to a whispering gallery mode is shown in Fig. 19.22 where anti-crossing behavior is observed at low temperatures. Tuning is achieved by temperature variation. Behavior of a similar system in the weak coupling regime is shown in Fig. 19.24.

19.2.2   Purcell Effect

According to Fermi's golden rule (19.1), the probability of an optical transition depends on the density of available optical modes (final states). If the density of modes is enhanced compared to its vacuum value (19.2) at a resonance of an optical cavity, the lifetime of the electronic state decreases by the Purcell factor [1374]

$$F_{\mathrm{P}} = \frac{3}{4\pi^2} \, Q \, \frac{(\lambda/n)^3}{V},$$
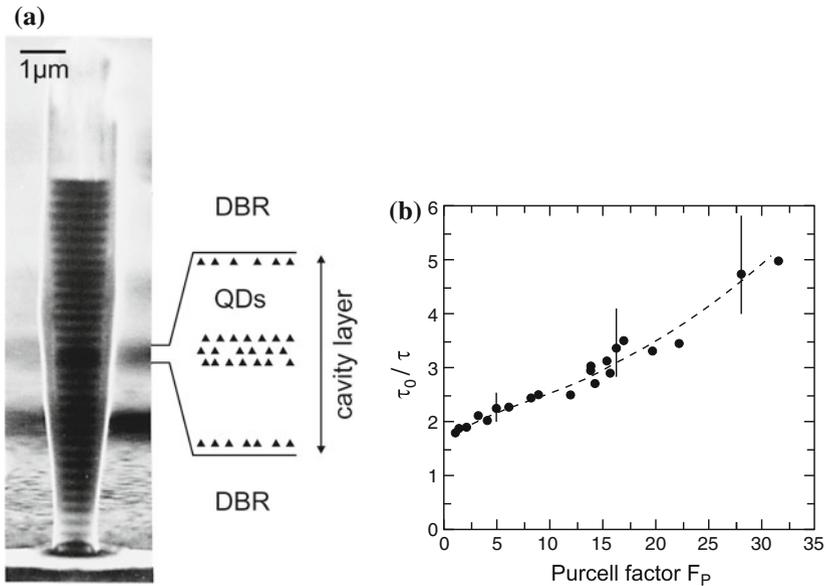(19.48)

(a)

Fig. 19.23 (**a**) Micropillar with MBE-grown GaAs/AlAs DBRs and a cavity containing five layers of InAs quantum dots as indicated. The pillar has been prepared by reactive ion etching. Reprinted with permission from [1375], ©1998 APS. (**b**) Experimental decay time τ of on-resonance quantum dot luminescence scaled by off-resonance lifetime $\tau_0 = 1.1$ ns (close to lifetime in a QD in bulk) for a variety of micropillars with different Purcell factors F_P. The *error bars* correspond to the measurement accuracy of the decay time (± 70 ps), the *dashed line* is a guide to the eye. Adapted from [1375]

where n is the refractive index of the medium, Q is the quality factor of the cavity resonance and V is the effective mode volume.[3] Experiments on the emission of quantum dots (that generally provide small absorption and thus allow for the weak coupling regime) in etched micropillars containing a microcavity (Fig. 19.23a) have shown that indeed the luminescence decay is faster for cavities with large Purcell factor (Fig. 19.23b) [1375]. The resonance of cavity mode and emitter leads to an enhanced emission intensity as shown in Fig. 19.24 for the exciton emission of a single quantum dot in a microdisc [1376].

19.2.3 Deformed Resonators

The whispering gallery modes in circular (or spherical) cavities are long-lived and emission goes into all angles. Light escape is based only on the exponentially slow

---

[3] V is given by the spatial integral of the vacuum field intensity for the cavity mode, divided by its maximum value.
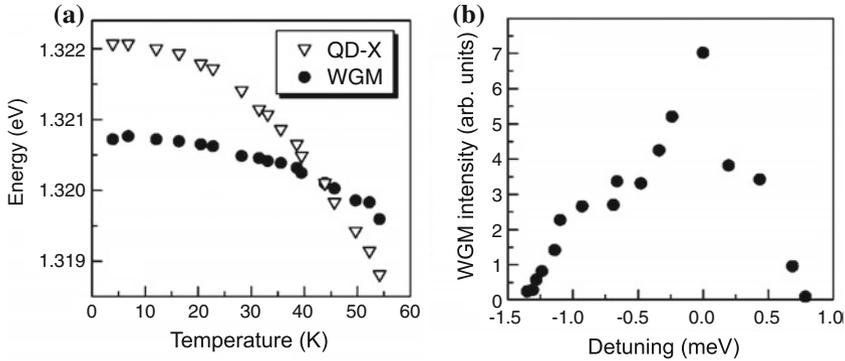
Fig. 19.24 (**a**) Temperature dependence of the energy positions of the whispering gallery mode (WGM) of a 5-µm diameter AlGaAs/GaAs microdisc ($Q = 6500$) and the single-exciton resonance of a single InAs quantum dot contained within the disc. (**b**) Intensity of WGM mode as a function of the detuning $E_{WGM} - E_{QD-X}$ from the QD single exciton resonance. The excitation density was $15\,\mathrm{Wcm}^{-2}$ for all data. Adapted from [1376]

process of evanescent leakage (neglecting disorder effects such as surface roughness). In order to overcome the isotropic light emission, the resonator needs to be deformed. This can be accomplished with an ellipsoidal shape, i.e.

$$r(\phi) = R \left[1 + \epsilon \cos \phi \right], \tag{19.49}$$

where $1 + 2\epsilon$ is the aspect ratio of the ellipse. The increased radiation leads to a decrease of the Q-factor as shown in Fig. 19.21b. Also, a new decay process, refractive escape, becomes possible. A ray that is initially in a whispering gallery trajectory diffuses in phase space until finally an angle smaller than the critical angle for total reflection (9.11) is reached. The ray dynamics becomes partially chaotic [1377].

One other possible deformation of the circular disc geometry is a 'flattened quadrupole' as shown in Fig. 19.25a. This shape can be parameterized by a deformation parameter ϵ and the angle-dependent radius $r(\phi)$ given by

$$r(\phi) = R \left[1 + 2\,\epsilon \cos^2 (2\phi)\right]^{1/2}. \tag{19.50}$$

For small deformation, the whispering gallery modes become chaotic and exhibit preferred emission along the long axis of the resonator (Fig. 19.25b). For larger deformations ($\epsilon \geq 0.14$), a stronger and qualitatively different directionality occurs in the shape of a bow-tie [1378] as shown in Fig. 19.25c. The optical laser power extracted from deformed resonators was found to increase exponentially with ϵ; for $\epsilon = 0.2$ it was 50 times larger than for the circular resonator.

Another modification that can be applied to the microdisc in order to increase outcoupling of light, is the spiral resonator [1379] as shown in Fig. 19.26a. The radius is parameterized by
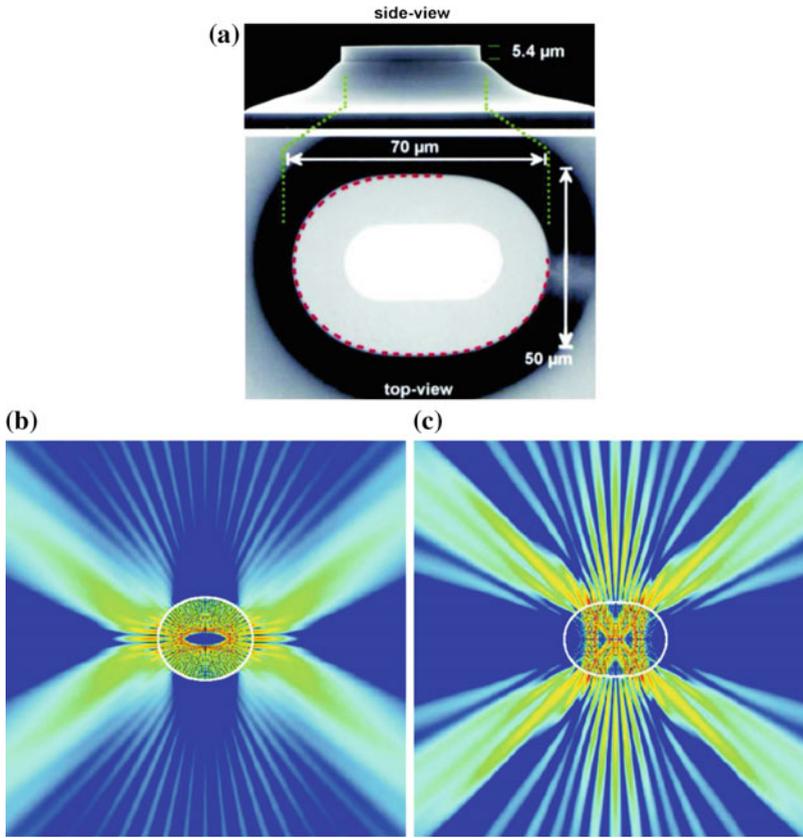
Fig. 19.25 (**a**) SEM image of a quadrupolar cylinder laser with deformation parameter $\epsilon \approx 0.16$ on a sloped InP pedestal. The *light grey area* in the top view is the electrical contact. (**b**) Simulated near-field intensity pattern of a chaotic whispering gallery mode for $\epsilon = 0.06$ and $n = 3.3$. (**c**) Simulated near-field intensity pattern of a bow-tie mode for $\epsilon = 0.15$. The length of the minor axis for (**b**) and (**c**) is $50\,\mu$m. Reprinted with permission from [1378], ©1998 AAAS

$$r(\phi) = R\left[1 + \frac{\epsilon}{2\pi}\,\phi\right]. \qquad (19.51)$$

The experimental emission pattern is displayed in Fig. 19.26b. It exhibits a maximum along the direction of the tangent at the radius step. The simulated near-field intensity of such an emission mode is shown in Fig. 19.26c. In a spiral laser, ray dynamics is also chaotic [1380].
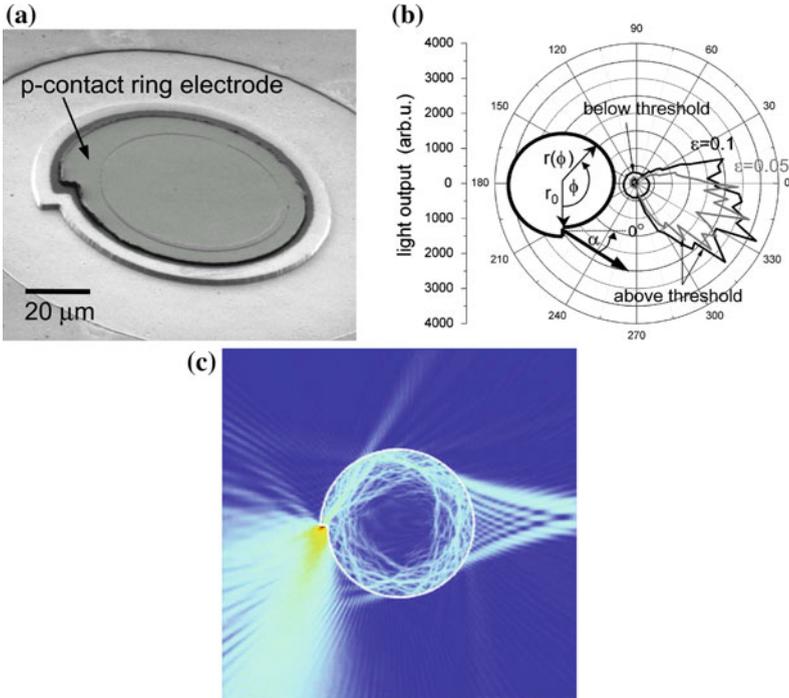
Fig. 19.26 (**a**) SEM image of a microcavity disc laser diode with a disc radius of 50 μm. The p-contact ring electrode defines the areas through which carriers are injected into the microdisc and where stimulated emission can take place. (**b**) Radial distribution of the light output from the spiral-shaped microdisc laser diode measured below and above threshold. The radius of the spiral microdisc was $r_0 = 250$ μm and the deformation parameters were $\epsilon = 0.05$ (*grey*) and $\epsilon = 0.10$ (*black*). An emission beam at an angle of $\alpha = 0°$ corresponds to a direction normal to the notch surface as shown in the *inset*. Below the laser threshold, the emission pattern is essentially isotropic and independent of the deformation parameter. Above the threshold, directional emission is clearly observed with the emission direction at a tilt angle $\alpha \approx 25°$. The measured divergence angle of the far-field pattern is $\sim 75°$ for $\epsilon = 0.10$ and $\sim 60°$ for $\epsilon = 0.05$. Reprinted with permission from [1381], ©2004 AIP. (**c**) Simulated near-field intensity pattern of an emission mode with $nkR \approx 200$ for deformation $\epsilon = 0.10$. Reprinted with permission from [1379], ©2003 AIP

19.2.4 Hexagonal Cavities

Hexagonal cavities develop, e.g., in microcrystals of wurtzite semiconductors (with the *c*-axis along the longitudinal axis of the pillar). In Fig. 19.27a, a ZnO tapered hexagonal resonator (needle) is shown. Whispering gallery modes modulate the
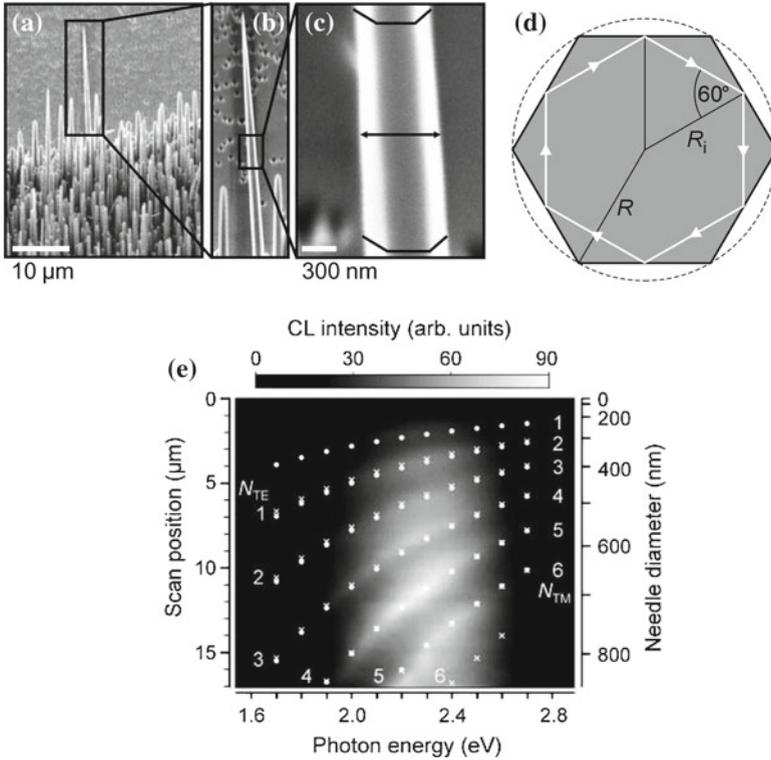
Fig. 19.27 (**a**)–(**c**) SEM images of ZnO nanoneedle fabricated by pulsed laser deposition. (**d**) Schematic geometry of cross-sectional plane. R_i (R) is the radius of the incircle (circumscribing circle). The circumference of the inscribed *white hexagon*, representing the path of a whispering gallery mode, has a length of $6R_i$. (**e**) Two-dimensional plot of spectra recorded along a linescan along the needle's longitudinal axis. The left vertical axis shows the linescan position x, the right one refers to the respective needle diameter D. The spectral maxima, i.e. the measured WGM energies, appear as bright belts going from the bottom left corner to the right upper one. With decreasing diameter, all resonances shift systematically to higher energies. The *white dots* give theoretical TM-resonance energy positions obtained from (19.52), *white crosses* give the same for TE-polarization. Reprinted with permission from [1382], ©2004 APS

intensity of the green ZnO luminescence [1382].[4] In a simple plane-wave model, the resonance condition is given by

$$6R_i = \frac{h\,c}{n\,E}\left[N + \frac{6}{\pi}\arctan\left(\beta\sqrt{3n^2 - 4}\right)\right], \qquad (19.52)$$

---

[4]We note that besides the green luminescence as in Fig. 10.20, an unstructured green band also occurs that is observed here. Its origin may be linked to the oxygen vacancy [1383].
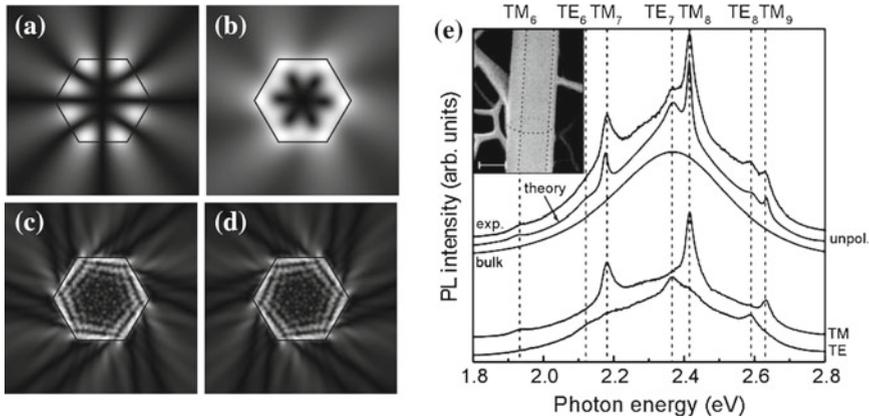
Fig. 19.28 Simulated near-field intensity pattern of modes in a cavity with hexagonal cross section (absolute value of electric field in linear grey scale): Modes ($N = 4$) with (**a**) symmetry $-a$ and (**b**) mode 4+ (nomenclature from [1384]) for $n = 2.1$ and $kR = 3.1553 - i0.0748$. Modes (**c**) 26− and (**d**) 26+ for $n = 1.466$ and $kR = 22.8725 - i0.1064$. The displayed modes have a chiral pattern. Emission originates mostly from the corners. (**e**) Micro-photoluminescence spectra of a single ZnO nanopillar. The three topmost curves are unpolarized. The curve labeled 'bulk' shows the unmodulated luminescence of the green luminescence in bulk. The line labeled 'exp.' shows the experimental μ-PL spectrum of the investigated nanopillar. The experimental spectra recorded for TM- and TE-polarization, respectively, are shown in the lowest two curves. The curve labeled 'theory' displays the theoretical luminescence spectra. *Dashed vertical lines* are guides to the eye referring to the spectral position of the dominating WGMs. The *inset* shows a SEM image of the investigated pillar, the scale bar has a length of 500 nm. The *dotted lines* show the position of the edges of the hexagonal resonator obtained from topography contrast
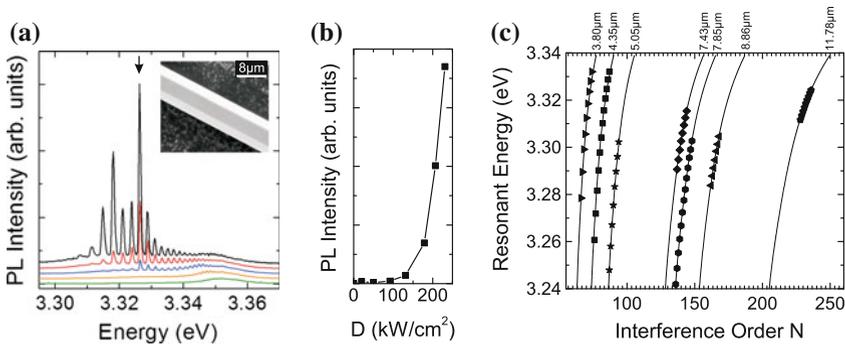

Fig. 19.29 (**a**) Photoluminescence spectra of a ZnO microwire with hexagonal cross section for various pump power densities (*lowest curve*: $D = 60$ kW/cm^2, *top curve*: $D = 250$ kW/cm^2) at $T = 10$ K. The inset shows the scanning electron microscopy image of a typical microwire ($d = 6.40$ μm). (**b**) Dependence of the emitted PL intensity of a selected lasing peak (denoted by an *arrow* in the spectrum in part (**a**)) on the excitation density D. *Lines* are guide to the eyes. (**c**) Dependence of the resonant energies on the interference order N for wires with different diameters as labeled on top of the graph. *Lines* are the predicted theoretical values calculated from (19.52) using diameter values obtained from SEM measurements; the *symbols* represent the experimentally observed peaks. Adapted from [1385]

where R_i is the radius of the inner circle (Fig. 19.27d), n is the index of refraction, N is the mode number and β is given by $\beta_{TM} = 1/n$ ($\beta_{TE} = n$) for TM (TE) polarization, respectively. Due to birefringence, $n_{\parallel}$ ($n_{\perp}$) has to be used as the index of refraction for TM (TE) polarization.

A $N = 26$ whispering gallery mode of a hexagonal resonator is shown in Fig. 19.28c, d. The 6-fold symmetric emission stems from the edges of the hexagon. While whispering gallery resonators have typically mode numbers $N \gg 1$, in such hexagonal resonators the whispering gallery modes could be followed down to $N = 1$ [1382] as shown in Fig. 19.27a, b, e.

Under high optical pumping laser action occurs on the whispering gallery modes. The peak positions, close to the band gap in the spectral region of the electron-hole plasma, follow (19.52) [1385], as shown for various diameters in Fig. 19.29. Pumping threshold even at room temperature is below $100\,\text{kW/cm}^2$ [1386].